Sensors and Materials, Vol. 36, No. 9 (2024) 3957–3980
MYU Tokyo

S & M 3778

Ground Control Point Chip-based Kompsat-3A Rational Polynomial Coefficient Bias Compensation Using Both Intensity- and Edge-based Matching Methods

Jaehong Oh,[1] DooChun Seo,[2] Jaewan Choi,[3] Youkyung Han,[4] and Changno Lee[4*]

[1]Department of Civil Engineering, Korea Maritime and Ocean University,
727 Taejong-ro, Yeongdo-gu, Busan 49112, Republic of Korea
[2]Korea Aerospace Research Institute, Gwahak-ro, Yuseong-Gu, Daejeon 34133, Republic of Korea,
[3]School of Civil Engineering, Chungbuk National University,
Chungdae-ro 1, Seowon-gu, Cheongju, Chungbuk 28644, Republic of Korea
[4]Department of Civil Engineering, Seoul National University of Science and Technology,
232 Gongneung-ro, Nowon-gu, Seoul 01811, Republic of Korea

(Received August 22, 2024; accepted September 17, 2024)

Keywords: RPCs, bias compensation, KOMPSAT, GCP chip, *NCC*, *RECC*, image matching

Recently, the number of high-resolution Earth-observing satellite sensors has been increasing owing to the growing needs of intelligence, mapping, and environmental monitoring. An acquired satellite image should be processed for analysis-ready data (ARD) that can be used for many applications. An important step among the processing is georeferencing that assigns geographic coordinates to each image pixel. These days, georeferencing is directly carried out using onboard sensors to produce sensor model information such as rational polynomial coefficients (RPCs). However, postprocessing is required to increase the positional accuracy of RPCs through bias compensation. Recently, bias compensation has been carried out on the basis of an automated process using ground control point (GCP) image chips. Image matching is carried out between the chips and the target satellite image to model the bias over the entire image. However, if the dissimilarity between the chip and the target satellite image increases owing to large differences in acquisition time and seasonal differences, the image matching often fails. Therefore, in this study, we utilized both intensity-based matching and edge-based matching to overcome these issues. We selected normalized cross-correlation (*NCC*) for intensity-based matching and relative edge cross-correlation (*RECC*) for edge-based matching. First, GCP chips were projected onto the target satellite images to align the two datasets. Then, both image matching methods were carried out in a pyramid image matching scheme, and their results were merged before RPC bias compensation with outlier removal. The experiments were carried out for two Kompsat-3A strips consisting of 9 and 7 scenes. *NCC* and *RECC* showed different matching results per scene, but *RECC* tended to show better results. *NCC* + *RECC* could derive most matching points, but the accuracy was between *NCC* and *RECC*. However, *NCC* + *RECC* shows potential to suppress a matching outlier. By applying automated bias compensation, 1.1–1.2 pixels of accuracy in root mean square error (*RMSE*) could be obtained.

*Corresponding author: e-mail: changno@seoultech.ac.kr
https://doi.org/10.18494/SAM5305

ISSN 0914-4935
https://myukk.org/

1. Introduction

The growing needs of intelligence, mapping, and environmental monitoring have increased the number of high-resolution Earth-observing satellite sensors worldwide. Satellite sensors such as WorldView, Pleiades, SPOT, Kompsat, SuperView, Satellogic, TripleSat, and CAS-500 are examples of Earth-observing satellites. These satellites provide a geospatial resolution of around 1 m to monitor target areas for many applications. Moreover, satellite constellations such as WorldView Legion, Dove of Planet, and Pathfinder of BlackSky provide abundant satellite images with more frequent revisit times.

High-resolution images from satellite sensors are not just photos but information. Therefore, they are considered as data or maps containing various information about the target. As analysis-ready data (ARD),[1] the image data must have accurate geographic coordinates. The process that assigns geographic coordinates onto each pixel is called georeferencing or registration. A satellite is installed with additional sensors such as global navigation satellite system (GNSS), inertial measurement unit (IMU), and a star tracker such that georeferencing is automatically carried out.[2] However, errors in the sensors produce inaccurate coordinates in the georeferencing; thus, postprocessing is required to increase the positional accuracy of rational polynomial coefficients (RPCs) through bias compensation.[3,4] Major commercial satellites such as WorldView and Pleiades are known to show 3–10 m positional errors in root mean square error (*RMSE*),[5,6] but other satellites show less accurate positional information. The accuracy is about 10 pixels or there are larger errors in the image coordinates such that the accuracy should be improved to one or two pixels of errors.[7]

RPCs as the main sensor model information must be bias-compensated using ground control points (GCPs). GCPs consist of 3D ground coordinates and the corresponding 2D image coordinates. Therefore, GCPs should be accurately measured both in the ground and also on the image. Note that the ground surveying of GCPs is limited owing to the cost and accessibility to the ground site. In addition, the manual image coordinate measurement is also labor-intensive, and the accuracy may vary for each human operator. Therefore, recently, GCP chips from accurately preconstructed geospatial data have been created[8–12] and used for bias compensation.[13–16] The image coordinate measurement was carried out by the image matching technique between the GCP chip and the target satellite image.

Conventional image matching is carried out using intensity within an area or features around the point of interest.[17,18] Area-based matching utilizes the correspondence of each pixel to compute correlation. Feature-based matching computes feature vectors around the area of interest and similarity between the vectors.[19–21] These methods are effective for images with high similarity such as stereo data acquired in less time difference between target images and slightly different acquisition angles. GCPs and target satellite images may or may not have similar acquisition seasons. Therefore, if the dissimilarity between the chip and the target satellite image increases owing to large differences in acquisition time and seasonal differences such as snow cover, image matching often fails.

The image matching between the GCP chip and the satellite image should be robust to the seasonal difference and land cover change. The digital number and feature vector within the area

of interest highly depend on the intensity directly affected by land cover. However, the edge information depends less on them. In particular, edge information around a human geographical feature such as a road or a land boundary is very strong and invariant to seasonal differences unless the land cover itself changes. However, edge information is not always abundant where natural geographical features are dominant. In this analogy, we utilized both intensity-based matching and edge-based matching to overcome the aforementioned issues. Normalized cross-correlation (*NCC*)[22] and relative edge cross-correlation (*RECC*)[23] were used for the methods because of their simplicity with low computational cost and decent performance compared with feature-based matching methods.

The proposed image matching method consists of three major steps. First, GCP chips are projected onto the target satellite images to align the two datasets. Second, both image matching methods were carried out. Third, their results were merged before RPC bias compensation with outlier removal. The first step is to use rather erroneous RPCs to project each pixel onto the target image. The projection generates a projected GCP chip with the same geospatial resolution as and a similar alignment to the target image. The erroneous RPCs locate the projected GCP chip on an inaccurate position in the target image. Therefore, in the second step, the image matching is carried out to find the correct position of the GCP chip in the target image. For each chip, both *NCC* and *RECC* are carried out to accept a better matching result. Using both approaches can produce more reliable matching results over the entire target image. The image matching is also carried out with an image pyramid for higher performance. The matching results are used for RPC bias compensation with the well-known affine model with outlier removal based on data snooping.

The experiments were carried out for two Kompsat-3A strips consisting of 9 and 7 scenes located in an inaccessible area where on-site surveying is limited. Using precreated satellite ortho images as GCP chips, we applied the *NCC* and *RECC* image matching methods with the pyramid scheme for bias compensation. Then, we compared the number of successful image matching and the bias modeling accuracy for each case.

This paper is structured as follows: The methodology is described in Sect. 2, experimental results for Kompsat-3A images are presented in Sect. 3, the discussion is presented in Sect. 4, and conclusions are provided in Sect. 5.

2. Methodology

The methodology is described as a flowchart in Fig. 1. Given the target satellite image and RPCs, GCP chips are projected onto the target image space using the rather erroneous RPCs. The projection generates the projected GCP chips that are distorted for sensor information and acquisition angles. The projected chips are now aligned with the target satellite image while the positional offset still exists for the RPC error. Therefore, the image matching is carried out to estimate the offset for each chip. To be robust to seasonal differences, both the *NCC* and *RECC* matching methods are carried out. In the matching stage, the image pyramid is used for more efficient and precise image matching by reducing the search range starting from the low-scale matching to the high-scale matching. The matching results from both image matching methods

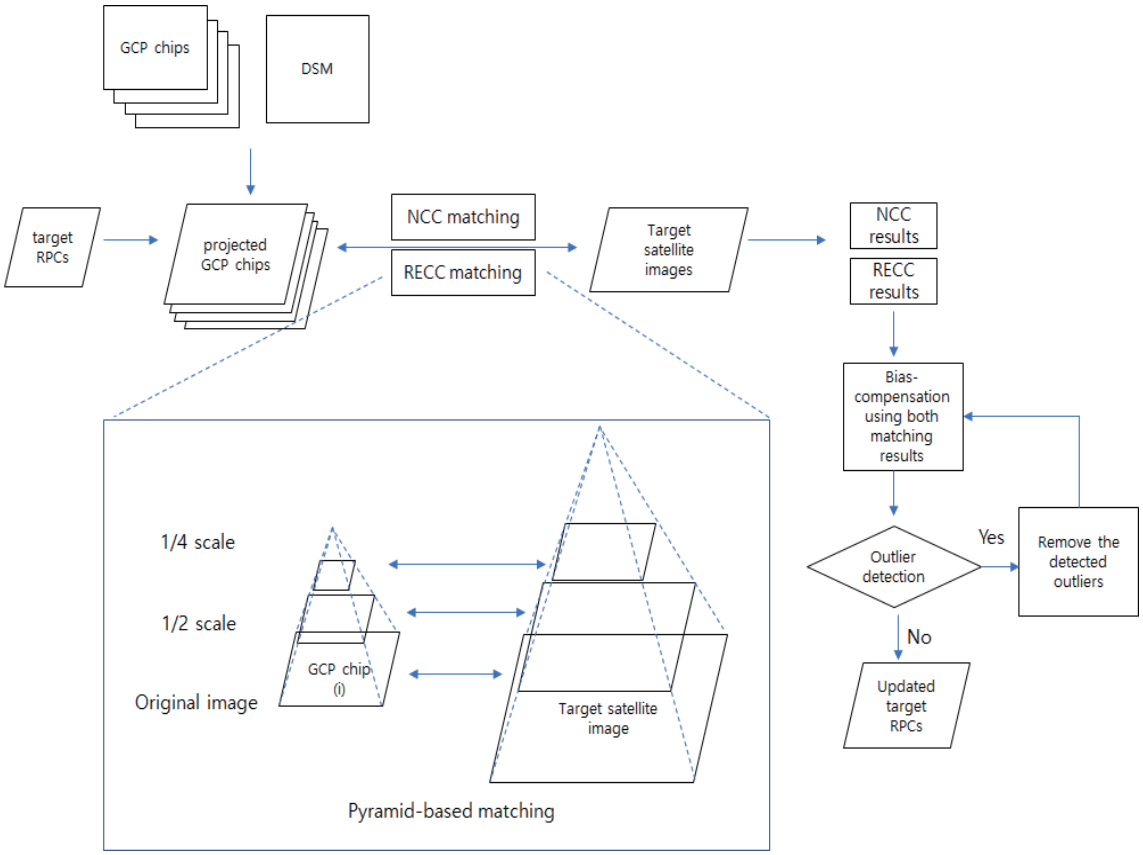

Fig. 1. (Color online) Flowchart of the study.

are now used for RPC bias compensation. In this stage, an outlier detection is iteratively applied until no outlier is detected. Finally, the filtered matching results are used for updated RPC generation.[24]

2.1 RPC bias compensation

As sensor model information, the rational function model (RFM) equation is given as Eq. (1) to use the ground coordinates (ϕ, λ, h) as an input for computing the image coordinates (l, s).[3] Eighty coefficients are required, i.e., 20 coefficients for each a, b, c, and d, which are called RPCs. The RPCs model the sensor information such as the focal length, sensor distortions, acquisition angles, errors in ephemeris of the platform, and topographic relief using the polynomial coefficients.

$$l = \frac{a^T u}{b^T u} L_S + L_O,\ s = \frac{c^T u}{d^T u} S_S + S_O \tag{1}$$

with

$$U = \frac{\phi - \phi_O}{\phi_S},\ V = \frac{\lambda - \lambda_O}{\lambda_S},\ W = \frac{h - h_0}{h_s}$$

$$u = \left[1 V U W VU VW UW V^2 U^2 W^2 UVW V^3 VU^2 VW^2 V^2 U U^3 UW^2 V^2 W U^2 W W^3\right]^T$$

$$a = \left[a_1\ a_2\ \cdots\ a_{20}\right]^T,\ b = \left[1\ b_2\ \cdots\ b_{20}\right]^T,\ c = \left[c_1\ c_2\ \cdots\ c_{20}\right]^T,\ d = \left[1\ d_2\ \cdots\ d_{20}\right]^T$$

Here, (ϕ, λ, h) are the geodetic latitude, longitude, and ellipsoidal height, respectively. (l, s) are the image row and column coordinates, respectively. (U, V, W) are the ground coordinates. (ϕ_o, λ_o, h_o) and (ϕ_S, λ_S, h_S S_S, L_S) are the offset and scale factors, respectively, for the latitude, longitude, height, column, and row.

The given RPCs are rather erroneous such that the computed image coordinates (l, s) are located in the wrong position. Therefore, an affine coordinate transform is widely used to compensate them, as shown in Eq. (2).[4] Finally, the more accurate position (l', s') can be computed.

$$l' = l + A_0 + A_1 l + A_2 s,\ \ s' = s + B_0 + B_1 l + B_2 s \tag{2}$$

Here, A_0, A_1, ..., B_2 are for an affine transformation that models shift, drift, and scale to angular affinity.

2.2 Image matching

NCC and *RECC* are simple but well-performed image matching methods. The computational cost is low and suitable for large satellite data processing. In addition, because the projected GCP chip and a target satellite image are already aligned, no feature-based matching with high computational cost is required.

NCC is an area-based matching methods using intensity values of corresponding image patches to compute the correlation between them as presented in Eq. (3) and Fig. 2. *A* is a target satellite image and *B* is a projected GCP chip. The reason why the GCP chips in the map

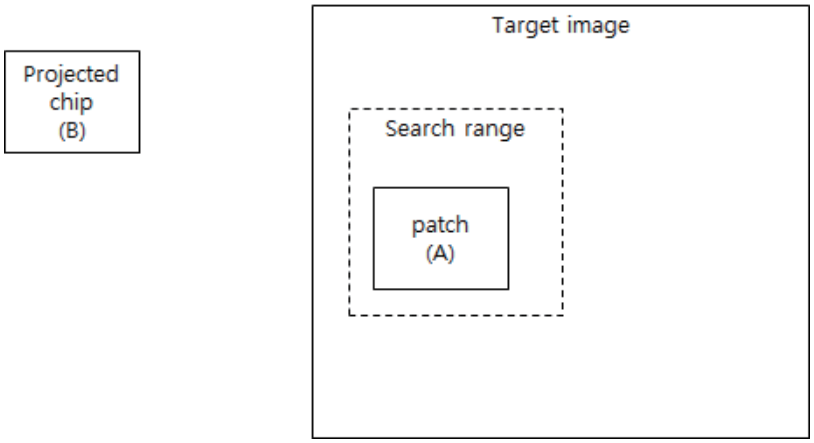

Fig. 2. Image patch in search range for image matching.

coordinates are not directly used for the image matching is that the satellite image is not in the map coordinates. Therefore, the GCP chips in the map coordinates are projected onto the satellite image coordinates. After the projection, the GCP chips and the target satellite image are well aligned for better image matching. The purpose of the image matching is that the correct location of B is searched within the search region in A using the indicator of *NCC*. *NCC* ranges from −1 to +1, and a larger *NCC* indicates that the corresponding patches are highly similar.

$$NCC = \frac{\sum_{i=1}^{w}\sum_{j=1}^{w}\left(B_{ij}-\overline{B}\right)\left(A_{ij}-\overline{A}\right)}{\sqrt{\left[\sum_{i=1}^{w}\sum_{j=1}^{w}\left(B_{ij}-\overline{B}\right)^2\right]\left[\sum_{i=1}^{w}\sum_{j=1}^{w}\left(A_{ij}-\overline{A}\right)^2\right]}} \tag{3}$$

Here, B is the projected GCP chip and A is a satellite image patch within the search region; both are in the size of $w \times w$. $\overline{B}, \overline{A}$ are averages of all intensity values in the patches.

RECC is an edge-based matching method using a sliding matching window similar to *NCC*. *RECC* uses an edge image that has 1 for edge and 0 for non-edge. The edge image can be generated using the well-known Canny operator.[25] The edge images A^e and B^e are generated from A, B, which are the target satellite image and projected GCP chip, respectively. *RECC* computes the number of overlapping edge pixels between A^e and B^e to measure the similarity and divides it by the total number of edge pixels as presented in Eq. (4). In other words, more overlapping edge pixels indicate better image overlapping. However, unlike *NCC*, *RECC* with no unit is not an absolute value because an image patch may contain a different number of edge pixels. Therefore, the peak position of high similarity can be identified using CV_4 that computes the closeness between the top four highest similarity positions as shown in Eq. (5). A small CV_4 indicates a successful matching position and the unit is pixels.[23]

$$RECC = \frac{\left(\sum_{i=1}^{w}\sum_{j=1}^{w}B_{ij}^{e}\times A_{ij}^{e}\right)}{\left(\sum_{i=1}^{w}\sum_{j=1}^{w}B_{ij}^{e}+\sum_{i=1}^{w}\sum_{j=1}^{w}A_{ij}^{e}\right)} \tag{4}$$

$$CV_4 = \frac{\left(\sum_{i=1}^{4}\sqrt{\left(r_{max}-r_i\right)^2+\left(c_{max}-c_i\right)^2}\right)}{4} \tag{5}$$

Here, B^e is a window in the edge image of the projected GCP chip (size: $w \times w$), A^e is an edge image of the target satellite image patch, and B_{ij}^e and A_{ij}^e are the digital numbers at row i and column j. CV_4 is the concentration based on the maximum to fourth largest *RECC* values, and (r_{max}) and (r_i, c_i) are the image coordinates of the positions of the maximum and i-th largest *RECC* values, respectively.

2.3 Outlier removal

Image matching produces outliers that should be detected and removed. The RPC bias compensation model in Eq. (2) is used for the detection in matrix form as shown in Eq. (6). RANdom SAmpling Consensus (RANSAC)[26] and data snooping[27] are well-known outlier removal techniques. RANSAC is based on random sampling and adequate for a large number of observations, whereas data snooping is based on a more rigorous statistical test by singling out each observation from the set. We used the data snooping algorithm because RANSAC may produce different results for each random sampling.

Data snooping utilizes the statistical T-test to determine whether the j-th observation is an outlier as shown in Eq. (7).

$$\underbrace{\begin{bmatrix} l'-l \\ s'-s \end{bmatrix}}_{y} = \underbrace{\begin{bmatrix} 1 & l & s & 0 & 0 & 0 \\ 0 & 0 & 0 & 1 & l & s \end{bmatrix}}_{X} \underbrace{\begin{bmatrix} A_0 & A_1 & A_2 & B_0 & B_1 & B_2 \end{bmatrix}^T}_{\xi} + e \tag{6}$$

$$T_j = \frac{R_j\left(2\times n - m - 1\right)}{\Omega - R_j}$$

$$\Omega = \tilde{e}^T\tilde{e},\ R_j = \frac{\left(\tilde{e}_j\right)^2}{r_j} \tag{7}$$

$$r_j = \left(\mathrm{I} - X\left(X^T X\right)^{-1} X^T\right)_{jj}$$

Here, $\tilde{e}$ is the residual vector computed from Eq. (6), $\tilde{e}_j$ is the j-th element, and n and m are the numbers of equations and unknowns, respectively. r_j is the redundancy number, X is the design matrix that consists of coefficients in front of unknowns in Eq. (6), and I is the identity matrix.

3. Results

3.1 Data

The experiments were carried out for two Kompsat-3A image strips that were acquired for inaccessible North Korea. The specifications of the tested data are listed in Table 1. The numbers

Table 1
Tested Kompsat-3A data specifications.

	Strip 1	Strip 2
Number of scenes	9	7
GCP chips	369	258
Data	2020-10-12	2021-04-06
Azimuth/off-nadir (degrees)	55.99/15.35	319.07/11.74
GSD (m)	0.59	0.57

of scenes per strip are 9 and 7. The acquisition dates are October 12, 2020 and April 6, 2021. The acquisition angles (off-nadir angles) range from 11.74 to 15.35 degrees. The azimuths are 55.99 and 319.07 degrees, which are mostly in the opposite direction to each other. Note that the larger off-nadir angle leads to the smaller ground sampling distance (GSD), and the tested data show a similar off-nadir angle resulting in a similar GSD. The positional accuracy of Kompsat-3A is known to be about 10 m (about 20 pixels) in *RMSE*.[28]

The site is mostly a rural area surrounded by mountains, as shown in Figs. 3 and 4. The data were acquired in the ascending node such that scene 1 is located in the south. Vegetation is

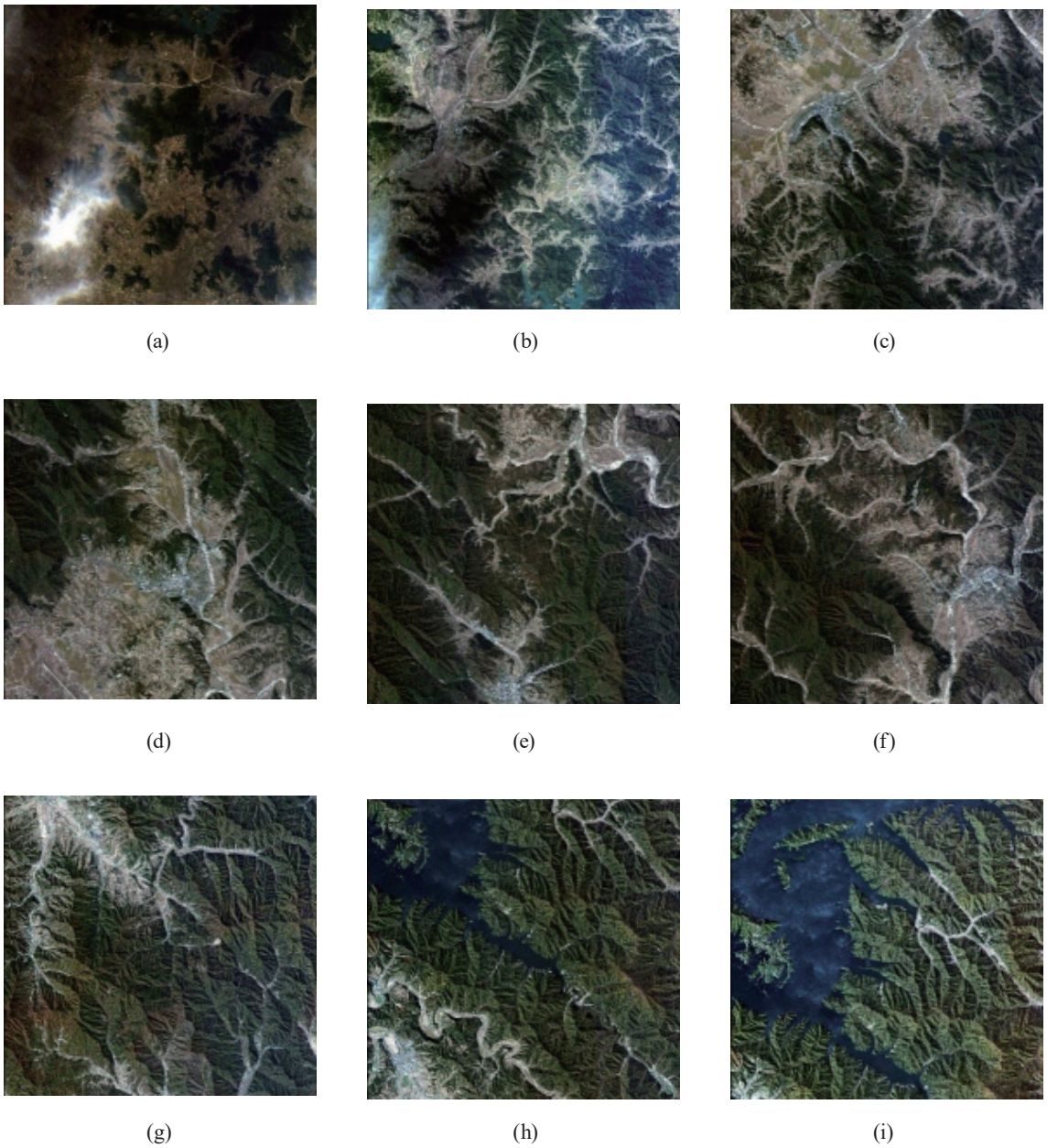

Fig. 3. (Color online) Tested Kompsat-3A data strip 1: (a) scene 1, (b) scene 2, (c) scene 3, (d) scene 4, (e) scene 5, (f) scene 6, (g) scene 7, (h) scene 8, and (i) scene 9.

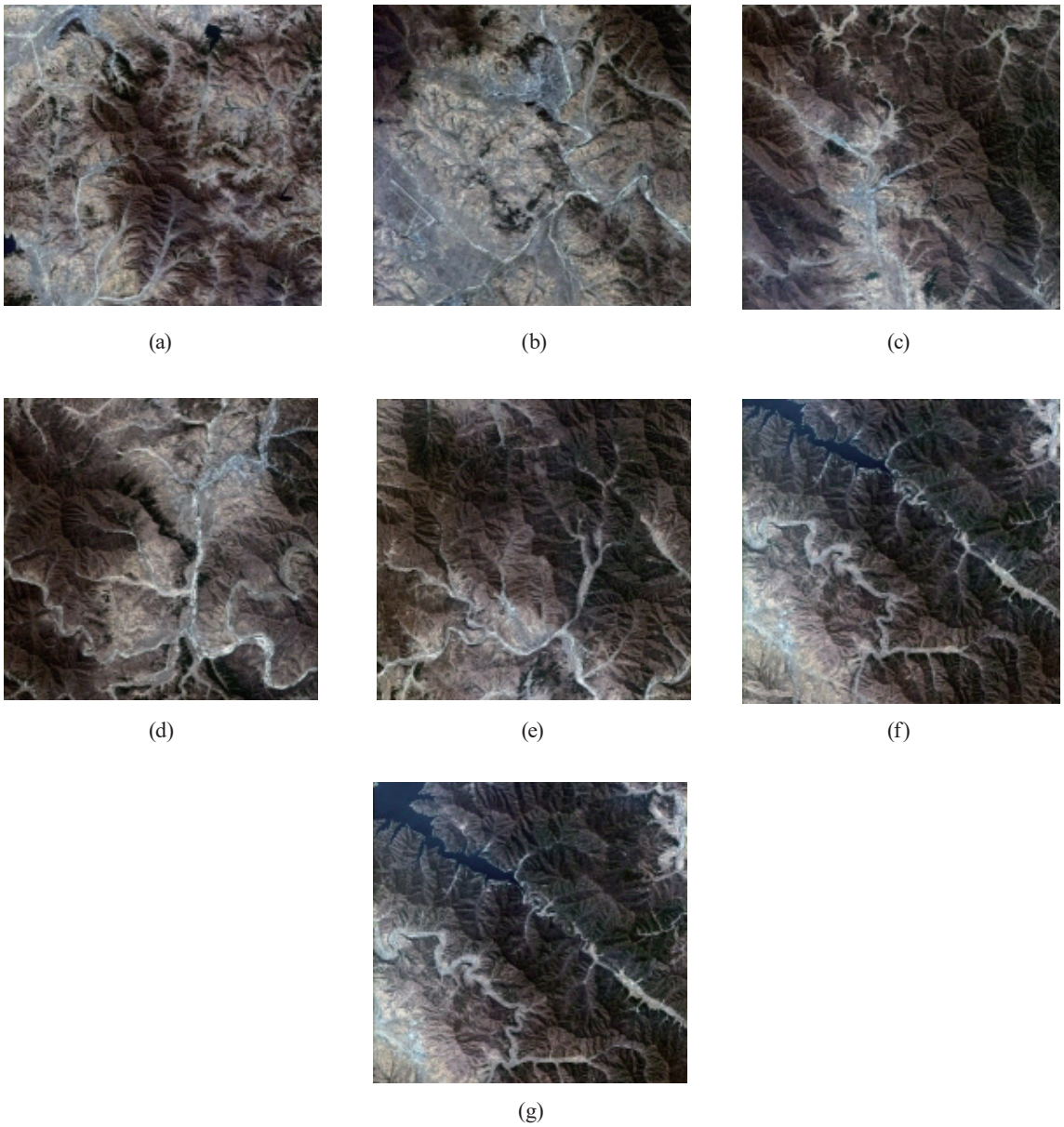

Fig. 4. (Color online) Tested Kompsat-3A data strip 2: (a) scene 1, (b) scene 2, (c) scene 3, (d) scene 4, (e) scene 5, (f) scene 6, and (g) scene 7.

healthy at the beginning of autumn (Fig. 3), while it is not at the end of winter (Fig. 4). Therefore, deciduous trees show different textures between the two datasets, as shown in Fig. 5.

3.2 Preparation and projection of GCP chips

GCP chips were created from panchromatic satellite ortho images of 1 m GSD. The spatial resolution of the chip is relatively lower than the target data because the data availability is limited for the target area in an inaccessible area. The chip size is 257 × 257 pixels. The horizontal coordinates are from the ortho image information, and the height information is derived from the associated 10-m-resolution digital terrain model (DTM).

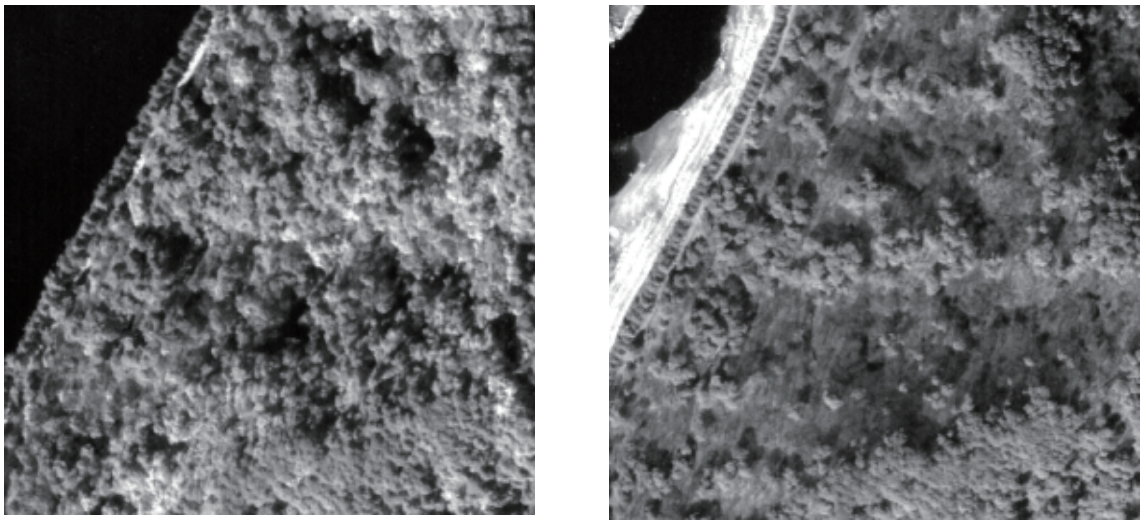

(a) (b)

Fig. 5. Texture difference between strips: (a) strip 1 and (b) strip 2.

Figure 6 depicts the distribution of the overall GCP chip distribution with the target image footprints over the sites. In strip 1, scenes 6–8 [Figs. 3(f)–3(h)] partially overlap and scenes 6 and 7 [Figs. 4(f) and 4(g)] mostly overlap in strip 2.

Each GCP chip is in the ground coordinate system because the source is an ortho image. A target image does not have coordinates because no georeferencing has been carried out, and all target images are not corrected for sensor distortion, acquisition angles, and topographic reliefs. Therefore, the alignment between the chip and the target image is dissimilar. For easier and higher image matching performance, a GCP chip is projected onto the target image space using the given RPCs. Even if the RPCs are rather erroneous, the positional accuracy is usually less than dozens of meters, and the RPCs can apply the sensor distortion, acquisition angles, and topographic reliefs to the chips for alignment. Figure 7 presents examples of chip projections for each strip. The projection rotates and distorts the chip similar to the target images. The boundary of the projected chip shows that a different geometry of each strip is applied to the chips. The upper chip in Fig. 7 is decent with invariant features, whereas the lower chip shows an example with poor geographical features for image matching. In addition, looking at the lower chips, we can observe that the projected chip is more similar to target strip 2 than the original GCP chip.

3.3 Image matching with RPC bias compensation

Given a projected GCP chip and the computed target image coordinates from the erroneous RPCs, the correct location of the GCP chip is sought by image matching. The search range is established using typical Kompsat-3A positional errors. About 20 pixels of error in *RMSE* was reported,[28] such that we used 100 pixels considering that large errors may occur. The image matching with the large search range is computationally ineffective, and it may introduce matching errors as Fig. 8 depicts the matching with a search range of 100 pixels.

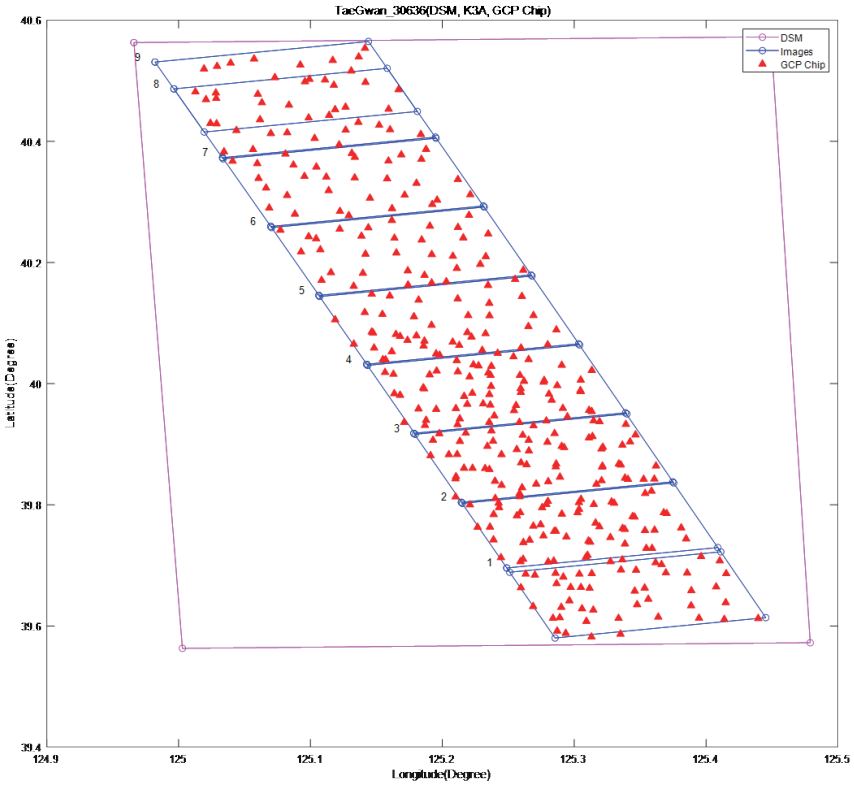

(a)

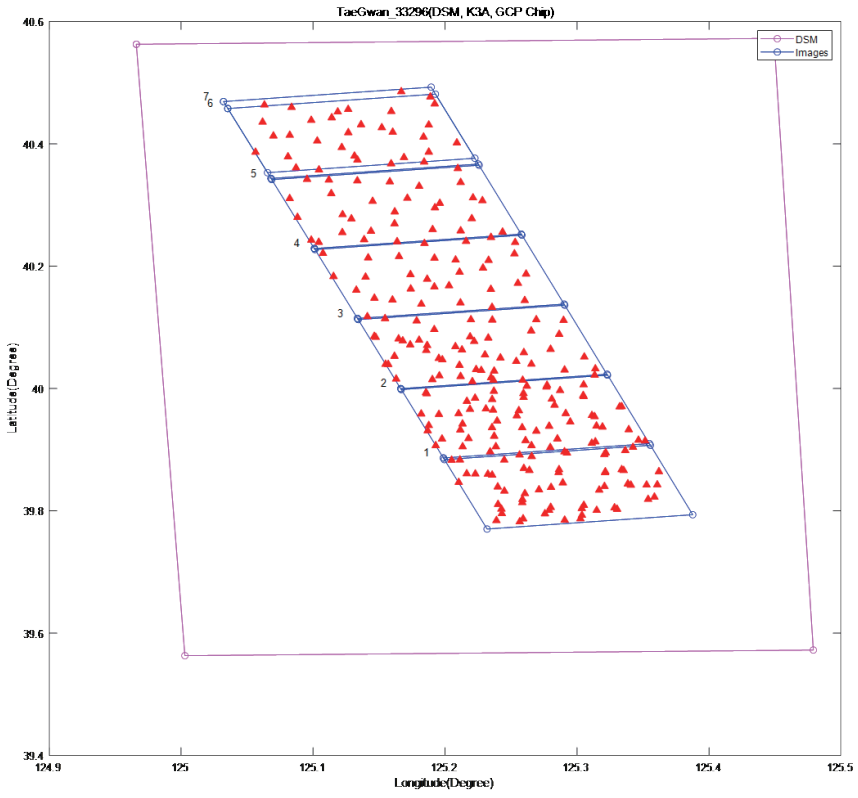

(b)

Fig. 6. (Color online) Data distribution with GCP chips in map coordinate systems: (a) strip 1 and (b) strip 2. Triangles indicate the location of GCP chips.

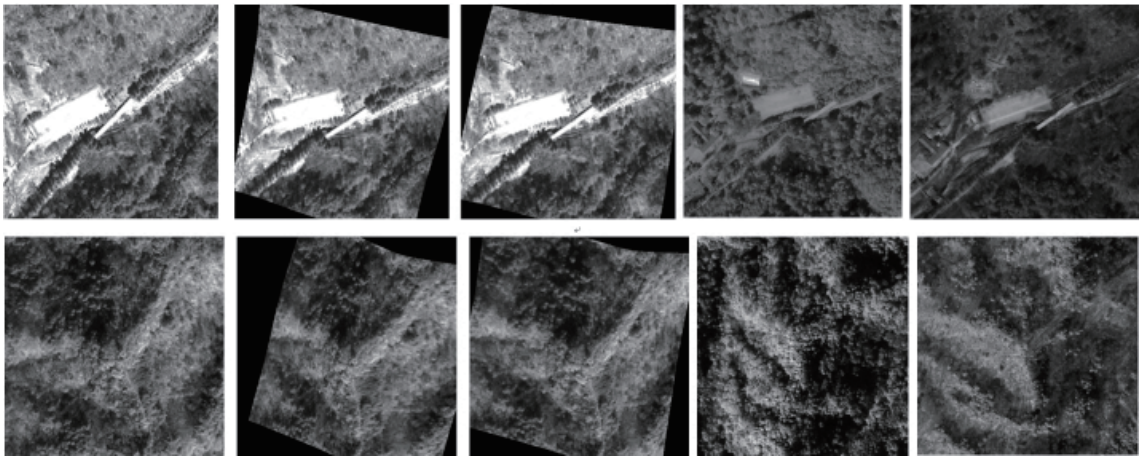

(a) (b) (c) (d) (e)

Fig. 7. (Color online) Examples of projected GCP chips: (a) ortho chips in map coordinate systems, (b) projected chips (strip 1), (c) projected chips (strip 2), (d) target satellite strip 1, and (e) target satellite strip 2.

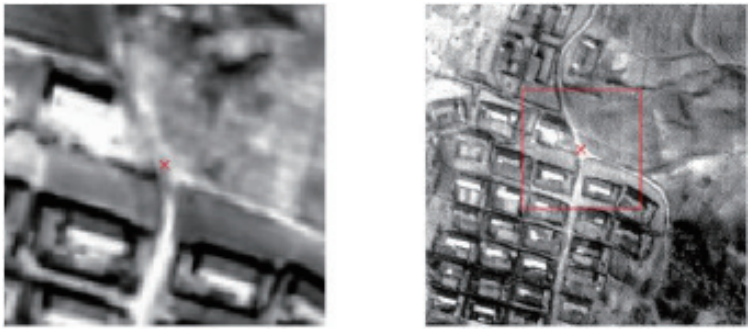

(a) (b)

Fig. 8. (Color online) Example of image matching with a search range of 100 pixels: (a) projected GCP chip and (b) target image with matched position.

Therefore, we used a pyramid-based image matching to effectively reduce the range. First, we changed the number of pyramid levels to select the optimal level. As shown in Fig. 9, level 3 (1/4 scale) was selected as the lowest scale for image matching.

Finally, 1/4- and 1/2-scale GCP chips and the corresponding target images were generated for image matching. The image matching was carried out at 1/4 scale with a 25 pixel search range (100 pixels in 1/1 scale), and if it is decent, the location was transferred to 1/2 scale and 1/1 scale matching with the reduced search range, as depicted in Fig. 10.

For stereo matching based on *NCC*, the matching window size is 7–11 pixels. However, for heterogeneous data, a larger matching window size should be used to include more feature information. As the window size increases, *NCC* tends to decrease. Therefore, the size of 50 by 50 pixels is used. For *RECC*, 180 by 180 pixels are used to include much edge information.

Figure 11 shows an example of poor *NCC* and decent *RECC*. In Fig. 11(a), the left is a chip, and the right is the target image with a wrong matched location. In Fig. 11(b), *RECC* finds a

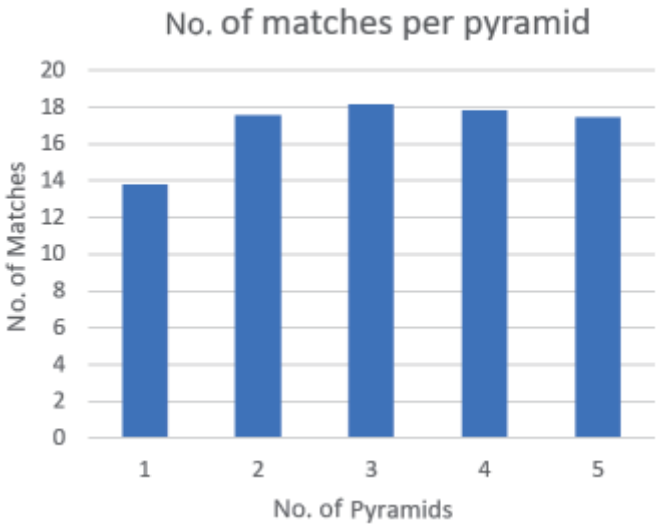

Fig. 9. (Color online) Number of matches per number of pyramids .

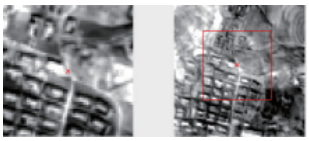

(a)

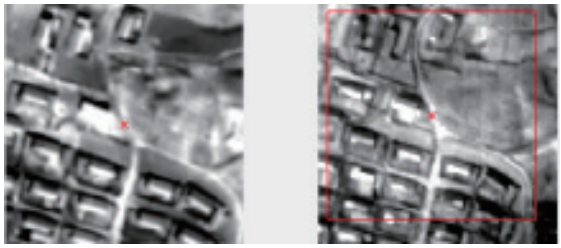

(b)

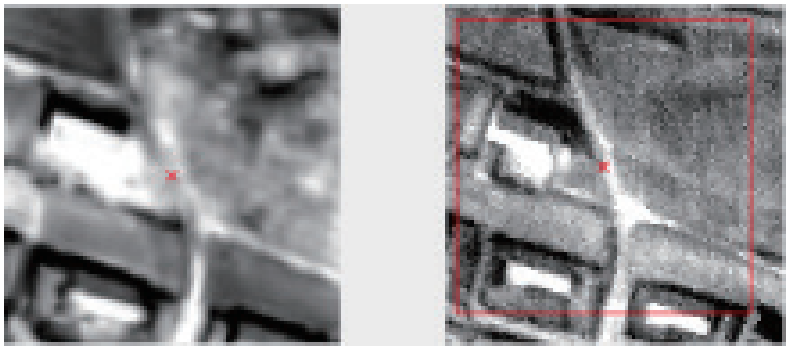

(c)

Fig. 10. (Color online) Image matching with pyramid to reduce the search range: (a) 1/4 scale, (b) 1/2 scale, and (c) 1/1 scale. Left: projected GCP chips, right: location on the target satellite image.

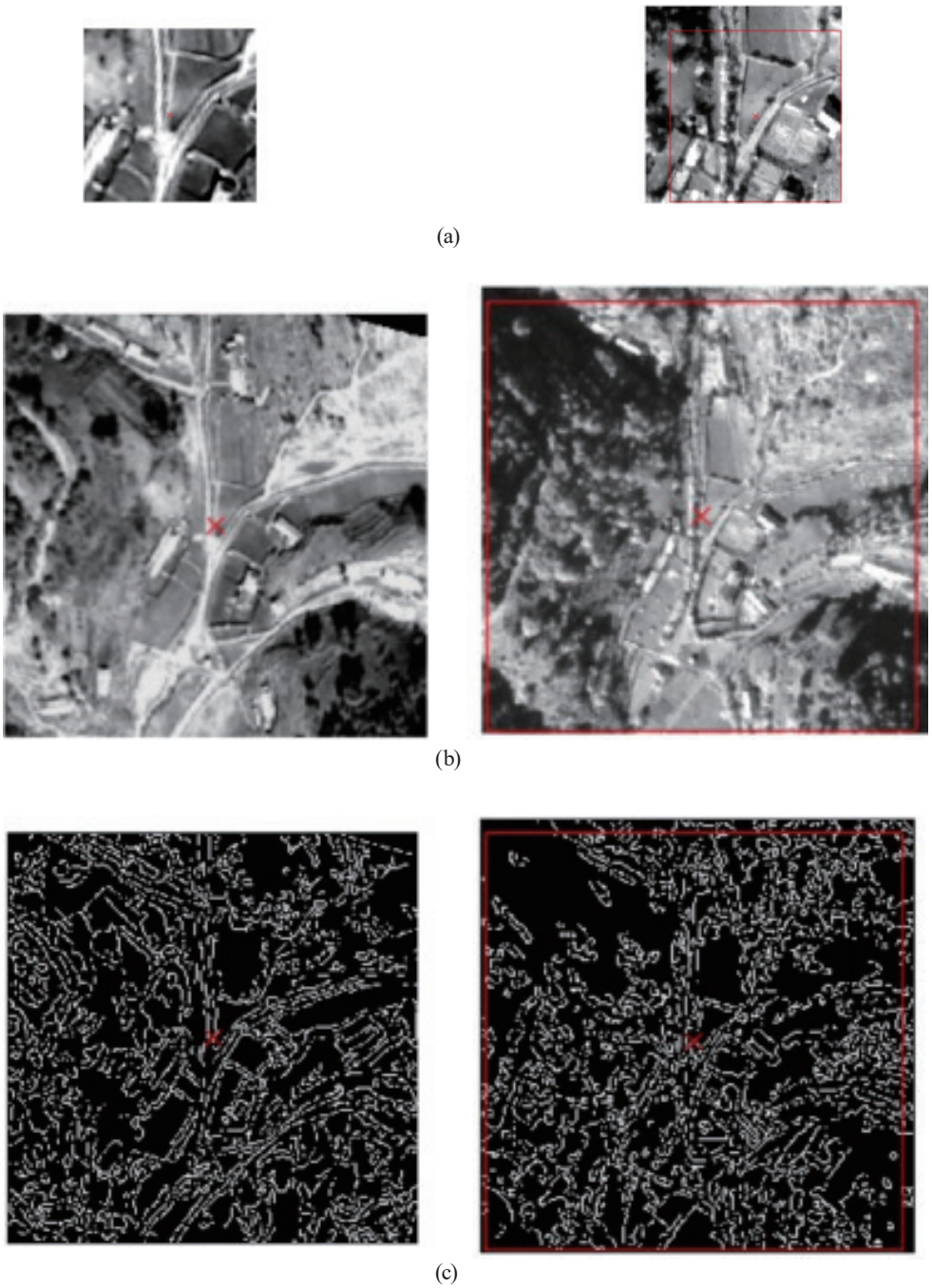

Fig. 11. (Color online) Example of poor NCC and decent RECC: (a) NCC-left: chip, right: target; (b) RECC-left: chip, right: target; and (c) RECC-left: chip edge, right: target edge.

better location with the edge correspondence shown in Fig. 11(c). In contrast, Fig. 12 presents an example of decent *NCC* and poor *RECC*.

Table 2 shows the number of image matchings per method for strip 1. Note that the number of points is counted after the outlier removal that may remove some points with moderate matching

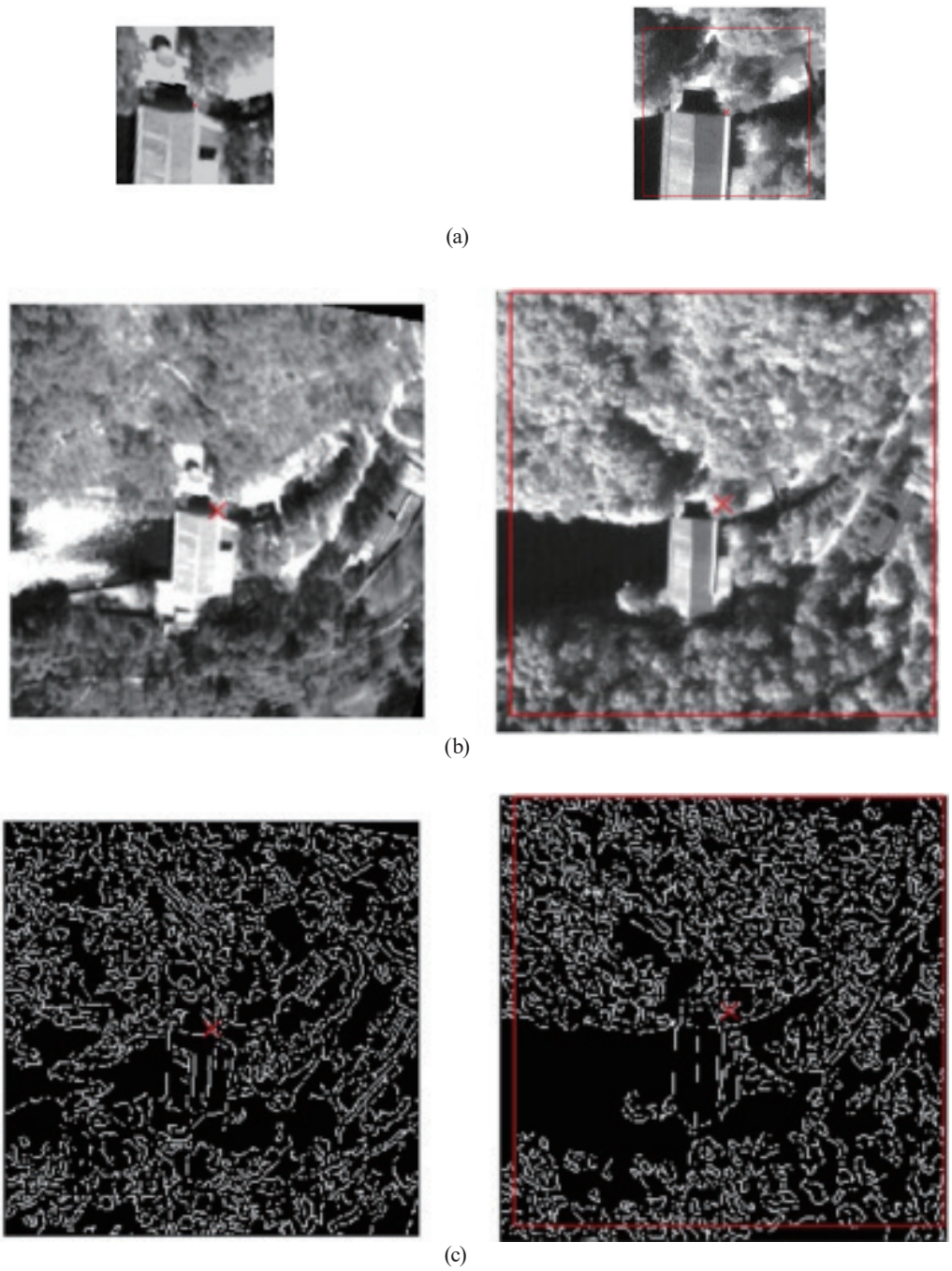

Fig. 12. (Color online) Example of decent NCC and poor RECC: (a) NCC-left: chip, right: target; (b) RECC-left: chip, right: target; and (c) RECC-left: chip edge, right: target edge.

quality if they do not pass the strict statistical testing. *NCC* produced 7–24 matching points with a mean of 14.9, and a mean success rate of 36.1%. *RECC* produced 8–37 points with a mean of 19.1 and a success rate of 42.8%. *NCC* + *RECC* (case 1) produced 8–37 points with a mean of 19.8 and a success rate of 45.0%. Overall, *RECC* produces more matching points than *NCC*

Table 2
Number of image machings and success rate (%) of image matching (strip 1).

Scene ID	Num. of GCPs per image	*NCC*	*RECC*	*NCC* + *RECC* Case 1	*NCC* + *RECC* Case 2
1	42	9 (21.4%)	16 (38.1%)	19 (45.2%)	18 (42.9%)
2	54	18 (33.3%)	32 (59.3%)	28 (51.9%)	27 (50.0%)
3	59	19 (32.2%)	37 (62.7%)	37 (62.7%)	36 (61.0%)
4	56	24 (42.9%)	27 (48.2%)	27 (48.2%)	30 (53.6%)
5	39	14 (35.9%)	22 (56.4%)	25 (64.1%)	24 (61.5%)
6	33	7 (21.2%)	12 (36.4%)	10 (30.3%)	10 (30.3%)
7	31	18 (58.1%)	9 (29.0%)	12 (38.7%)	11 (35.5%)
8	32	18 (56.3%)	8 (25.0%)	12 (37.5%)	8 (25.0%)
9	30	7 (23.3%)	9 (30.0%)	8 (26.7%)	8 (26.7%)
Mean		14.9 (36.1%)	19.1 (42.8%)	19.8 (45.0%)	19.1(42.9%)

because it is more invariant to the acquisition date difference between the chip and the target image. In addition, *NCC* + *RECC* tends to produce more points, but the increase was not considerable because a point with both successful *NCC* and *RECC* matchings counts as one. By removing less reliable points and retaining a similar number of points to *RECC*, case 2 results are derived. Case 2 shows the similar number of matched points and success rate to *RECC*.

Figure 13 shows the distribution of matched points for scene 1 in strip 1. The different distribution pattern between *NCC* and *RECC* is notable, and *NCC* + *RECC* consists of the results from the two methods. Some *NCC* and *RECC* points are added or removed in *NCC* + *RECC*. This depends on whether they are filtered or not in the outlier removal process during the RPC bias compensation.

In case 2, the number of matched GCPs consists of the numbers of *NCC* and *RECC* points as shown in Table 3. Note that no single method dominates the matching results.

Table 4 shows the results of the test on strip 2, which are similar to those of the test on strip 1. *NCC* produced 8–30 matching points with a mean of 17.7, and a mean success rate of 44.1%. *RECC* produced 12–30 points with a mean of 20.0 and a success rate of 50.6%. *NCC* + *RECC* produced 13–37 points with a mean of 22.7 and a success rate of 58.9%. Overall, *NCC* + *RECC* could generate the higest number of matching points, although the increase was not considerable.

NCC + *RECC* obtains more matching points than the others such that less reliable points could be removed, retaining a similar number of points to *RECC*, that is, case 2 in Tables 2 and 4.

In case 2, the number of matched GCPs consists of the numbers of *NCC* and *RECC* points as shown in Table 5. Note that no single method dominates the matching results.

Matching results are used for RPC bias compensation. Table 6 shows the affine-based bias compensation model residual after the outlier removal. *RMSE* is calculated down to the first decimal place. For image strip 1, *NCC* produced the highest accuracy for scenes 1, 2, 3, 5, 6, and 9. However, *NCC* produced significantly low results for scenes 7 and 8, which are harmful for georeferencing. *RECC* produced the highest accuracy for scenes 1, 7, and 8. Also, *RECC* could secure stable accuracy for problematic scenes 7 and 8, but it showed relatively low accuracy for scenes 6 and 9. In contrast, *NCC* + *RECC* tends to show smoothed accuracy between *NCC* and *RECC* except for scenes 4 and 9. From the mean, the overall *NCC* + *RECC* showed the most

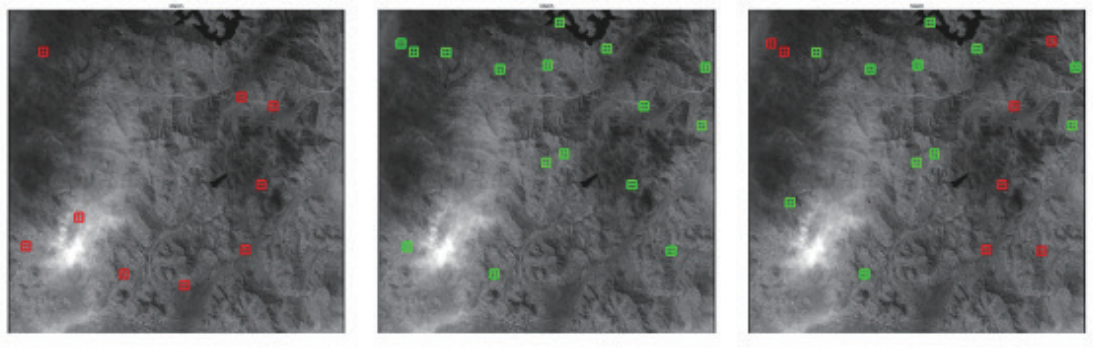

(a) (b) (c)

Fig. 13. (Color online) Matching point distribution for scene 1 (strip 1): (a) *NCC*, (b) *RECC*, and (c) *NCC* + *RECC*.

Table 3
NCC + *RECC* matching (strip 1).

Scene ID	*NCC* + *RECC* Case 2	Num. of *NCC*	Num. of *RECC*
1	18 (42.9%)	7 (16.7%)	11 (26.2%)
2	27 (50.0%)	16 (29.6%)	11 (20.4%)
3	36 (61.0%)	18 (30.5%)	18 (30.5%)
4	30 (53.6%)	20 (35.7%)	10 (17.9%)
5	24 (61.5%)	13 (33.3%)	11 (28.2%)
6	10 (30.3%)	8 (24.2%)	2 (6.1%)
7	11 (35.5%)	4 (12.9%)	7 (22.6%)
8	8 (25.0%)	5 (15.6%)	3 (9.4%)
9	8 (26.7%)	2 (6.7%)	6 (20.0%)

Table 4
Number of image machings and success rate (%) of image matching (strip 2).

Scene ID	Num. GCPs per image	*NCC*	*RECC*	*NCC* + *RECC* Case 1	*NCC* + *RECC* Case 2
1	57	21 (36.8%)	28 (49.1%)	29 (50.9%)	31 (54.4%)
2	55	30 (54.5%)	28 (50.9%)	37 (67.3%)	32 (58.2%)
3	46	29 (63.0%)	30 (65.2%)	32 (69.6%)	28 (60.9%)
4	29	10 (34.5%)	12 (41.4%)	15 (51.7%)	14 (48.3%)
5	28	8 (28.6%)	12 (42.9%)	13 (46.4%)	9 (32.1%)
6	29	14 (48.3%)	17 (58.6%)	18 (62.1%)	19 (65.5%)
7	28	12 (42.9%)	13 (46.4%)	18 (64.3%)	15 (53.6%)
8	57	21 (36.8%)	28 (49.1%)	29 (50.9%)	31 (54.4%)
9	55	30 (54.5%)	28 (50.9%)	37 (67.3%)	32 (58.2%)
	Mean	17.7 (44.1%)	20.0 (50.6%)	22.7 (58.9%)	21.1 (53.3%)

Table 5
NCC + *RECC* matching (strip 2).

Scene ID	*NCC* + *RECC* Case 2	Num. of *NCC*	Num. of *RECC*
1	31 (54.4%)	16 (28.1%)	15 (26.3%)
2	32 (58.2%)	23 (41.8%)	9 (16.4%)
3	28 (60.9%)	8 (17.4%)	20 (43.5%)
4	14 (48.3%)	11 (37.9%)	3 (10.3%)
5	9 (32.1%)	5 (17.9%)	4 (14.3%)
6	19 (65.5%)	10 (34.5%)	9 (31.0%)
7	15 (53.6%)	8 (28.6%)	7 (25.0%)

Table 6
Compensation precision in RMSE [pixels] (strip 1).

Scene ID	*NCC*			*RECC*			*NCC + RECC* Case 1			*NCC + RECC* Case 2		
	Sample	Line	Diagonal	Sample	Line	Diagonal	Sample	Line	Diagonal	Sample	Line	Diagonal
1	0.9	0.8	1.1	0.9	0.7	1.1	0.8	0.8	1.1	0.8	0.8	1.1
2	0.9	0.9	1.3	1.1	1.0	1.5	0.9	0.9	1.3	0.9	0.9	1.3
3	0.8	0.6	1.0	0.8	0.9	1.2	0.8	0.9	1.2	0.7	0.9	1.1
4	0.9	0.8	1.2	0.9	0.8	1.2	0.8	0.7	1.1	0.9	0.7	1.2
5	0.8	0.8	1.1	1.0	0.7	1.2	0.9	0.9	1.3	0.8	0.7	1.1
6	0.6	0.2	0.7	1.6	1.2	1.9	0.6	0.4	0.7	0.6	0.4	0.7
7	3.1	2.8	4.2	0.9	0.9	1.2	0.9	0.9	1.3	0.7	0.9	1.2
8	2.7	2.8	3.9	0.5	0.7	0.9	1.0	1.3	1.7	0.6	0.7	0.9
9	0.7	0.6	0.9	1.4	1.0	1.7	0.4	0.7	0.9	0.4	0.7	0.9
Mean	1.3	1.1	1.7	1.0	0.9	1.3	0.8	0.9	1.2	0.7	0.7	1.1
Max	3.1	2.8	4.2	1.6	1.2	1.9	1.0	1.3	1.7	0.9	0.9	1.3

stable accuracy even though the increase was minimal up to 0.1–0.2 pixels compared with that of *RECC*. *NCC + RECC* helps to suppress the low accuracy modeling by two methods compensating each other. In case 2 by removing less reliable points and retaining a similar number of points to *RECC*, the maximum error dropped from 1.9 to 1.3 pixels.

For strip 2, *NCC* produced a low accuracy for scene 3 in Table 7. Overall, *RECC* showed the highest accuracy even though the difference was negligible (0.1–0.2 pixels) compared with *NCC + RECC*. Fortunately, there are no significantly low accurate results found in *RECC* in this strip. In case 2, by removing less reliable points and retaining a similar number of points to *RECC*, the maximum error of *NCC + RECC* dropped to 1.3 pixels, which is a more negligible difference from *RECC*. Therefore, in strip 2, *RECC* was the best option, but the use of *NCC + RECC* can be another stable option to avoid potential low accurate results considering strip 1.

Tables 8 and 9 show the computed RPC bias in the target image for each strip and scene. Considering only the shift errors A0 and B0, the biases are up to more than 26 pixels, which is about 15 m on the ground. Considering this error, the original positional accuracy of the tested data seems within the reported value.[28] For strip 1, the bias before the RPC compensation is larger along the line direction than along the sample direction, while strip 2 shows a larger error along the sample direction. By compensating for these errors, one pixel level of RPC accuracy can be automatically obtained by GCP chip-based image matching.

Figure 14 shows a bias pattern from scene 1 of strip 1 along the line and sample directions. Figure 14(a) shows the line and sample biases along the line direction in the middle of the scene. The line direction bias and slope are larger than those of the sample direction. Figure 14(b) shows the bias along the sample direction in the middle of the line. The bias change along the sample direction is bounded to 2 pixels, whereas that along the line direction is up to 16 pixels. The bias change is much less along the sample direction than along the line direction. This shows that the bias modeling should not be carried out using the simple shift model, but the bias modeling of Kompsat-3A RPCs using the affine model is appropriate.

Table 7
Compensation precision in RMSE [pixels] (strip 2).

Scene ID	*NCC*			*RECC*			*NCC + RECC* Case 1			*NCC + RECC* Case 2		
	Sample	Line	Diagonal	Sample	Line	Diagonal	Sample	Line	Diagonal	Sample	Line	Diagonal
1	1.2	1.1	1.6	0.8	0.8	1.1	0.8	0.9	1.2	0.7	0.9	1.2
2	1.0	1.2	1.6	0.8	1.0	1.3	1.0	1.1	1.5	1.0	0.9	1.3
3	1.7	1.8	2.5	0.7	1.0	1.2	0.7	1.0	1.2	0.7	0.9	1.1
4	0.5	0.7	0.8	0.5	0.5	0.7	0.9	0.9	1.2	0.8	0.8	1.1
5	0.6	0.4	0.7	0.8	0.9	1.2	1.2	0.9	1.5	0.8	0.7	1.1
6	1.1	1.3	1.7	0.8	0.9	1.2	0.8	0.8	1.1	0.8	0.9	1.2
7	0.9	1.1	1.5	0.7	0.7	1.0	0.8	0.9	1.2	0.8	0.8	1.1
8	1.0	1.1	1.5	0.7	0.8	1.1	0.9	0.9	1.3	0.8	0.9	1.2
9	1.7	1.8	2.5	0.8	1.0	1.3	1.2	1.1	1.5	1.0	0.9	1.3
Mean	1.2	1.1	1.6	0.8	0.8	1.1	0.8	0.9	1.2	0.7	0.9	1.2
Max	1.0	1.2	1.6	0.8	1.0	1.3	1.0	1.1	1.5	1.0	0.9	1.3

Table 8
Estimated bias (strip 1).

Scenes	Bias					
	A0 (shift)	A1 (drift)	A2 (affinity)	B0 (shift)	B1 (drift)	B2 (affinity)
1	−17.635074	0.000060	0.000618	−4.709010	0.000071	0.000167
2	−26.809429	−0.000166	0.000417	−1.661388	−0.000065	0.000061
3	−18.838355	−0.000102	−0.000396	−1.932555	0.000089	−0.000069
4	−10.541562	−0.000117	−0.000258	−2.045777	0.000457	−0.000110
5	−1.245073	−0.000076	−0.000374	2.534880	0.000098	0.000002
6	2.011869	0.000002	−0.000248	−1.125922	0.000219	−0.000432
7	1.222146	−0.000054	0.000064	−1.416397	0.000204	0.000033
8	−3.585199	−0.000098	0.000263	0.318448	0.000176	−0.000176
9	0.951062	−0.000316	0.000182	−3.093446	0.000355	0.000058

Table 9
Estimated bias (strip 2).

Scenes	Bias					
	A0 (shift)	A1 (drift)	A2 (affinity)	B0 (shift)	B1 (drift)	B2 (affinity)
1	8.551921	−0.000072	0.000628	6.410667	0.000018	0.000453
2	−9.973537	−0.000084	0.000641	5.176177	0.000332	−0.000159
3	−12.649700	0.000100	−0.000049	12.887208	0.000186	−0.000225
4	−2.826613	−0.000155	−0.000279	12.478661	−0.000101,	0.000130
5	8.482035	−0.000115	−0.000483	20.834514	0.000051	−0.000384
6	5.875974	0.000135	−0.000027	16.941955	0.000169	0.000086
7	8.860162	0.000159	−0.000250	15.774101	0.000172	0.000135

Finally, the target images are orthorectified using the original erroneous and bias-compensated RPCs for comparison. Figure 15(a) shows the ortho images with the original erroneous and bias-compensated RPCs. Figure 15(a) also shows the ortho images of 2020 and 2021 with the original erroneous RPCs, and Fig. 15(b) shows those with the bias-compensated RPCs. The discrepancy between them (about 15 m) is clearly visible near buildings, whereas the compensated ortho image shows good registration results in Fig. 15(b). Building-level registration can be identified.

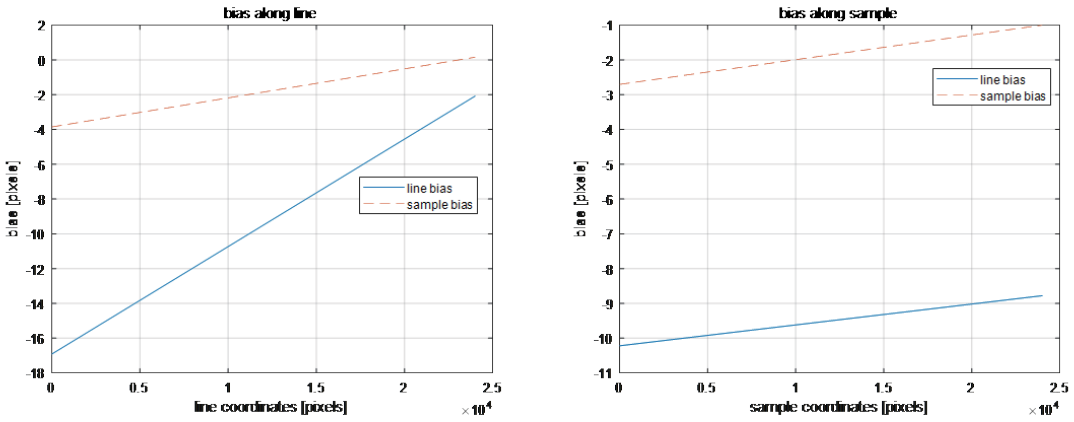

(a) (b)

Fig. 14. (Color online) Bias pattern of strip 1 – scene 1: (a) bias along line and (b) bias along sample.

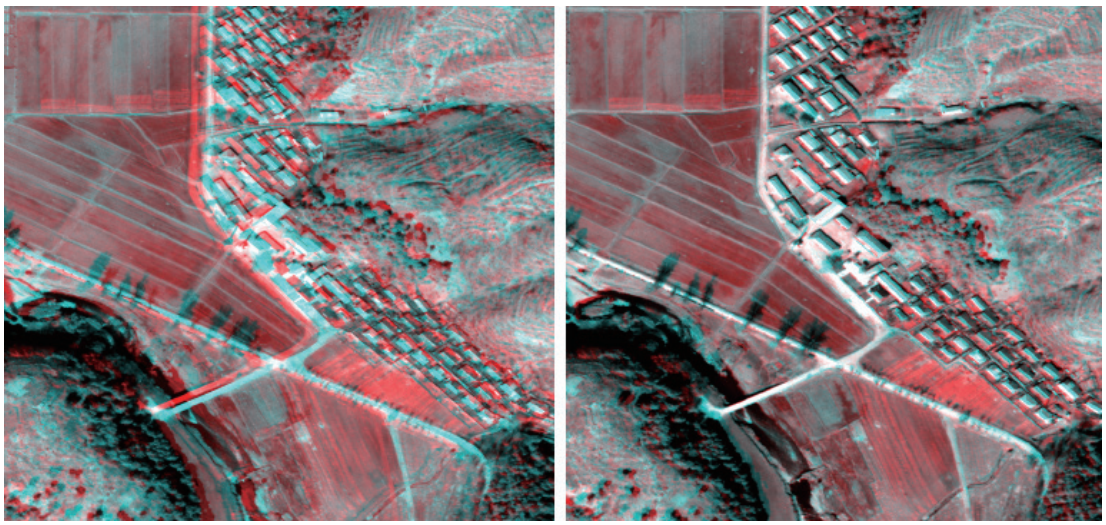

(a) (b)

Fig. 15. (Color online) Orthoimages overlay between 2020 and 2021 for registration comparison: (a) before and (b) after bias compensation.

4. Discussion

The accurate georeferencing of high-resolution satellite images is difficult and labor-intensive such that an automated but robust approach has been needed. To this end, the approach with image matching methods seems to have a high potential to reduce the cost.

NCC + *RECC* is recommended for more robust image matching by detecting and removing outliers because it can produce more redundant matching points than either *NCC* or *RECC*. Between *RECC* and *NCC*, the experimental results showed that *RECC* is more effective for heterogenous data matching than *NCC*.

We also applied feature-based matching methods such as SIFT and SURF to the experimental data; however, they were not only time-consuming but produced very poor results for these heterogenous data.

As a limitation of this study, the registration accuracy could not be assessed using a quality reference point with a reliable positional accuracy in the experiment. Since the tested GCP chips were derived from military data for the inaccessible area, metadata such as the accuracy and acquisition date were unknown. Therefore, the effect of the GCP quality as well as elevation accuracy on the image matching and RPC bias compensation could not be analyzed.

5. Conclusions

In this study, we used both the intensity- and edge-based matching methods for the automated RPC bias compensation and analyzed their performance for high-resolution satellite sensor data processing. To this end, *NCC* was selected for intensity-based matching and *RECC* was selected for edge-based matching. First, GCP chips were projected onto target satellite images to align the two datasets. Then, both image matching methods were carried out in a pyramid image matching scheme and their results were merged before RPC bias compensation with outlier removal. The experiments were carried out for two Kompsat-3A strips consisting of 9 and 7 scenes. The following conclusions were derived:

- Overall, *RECC* produces more matching points than *NCC* because it is more invariant to the acquisition date difference between the chip and the target image.
- *NCC* + *RECC* tends to produce more points even though the increase was not considerable because a point with both successful *NCC* and *RECC* matching counts as one.
- Bias modeling accuracy using *NCC* and *RECC* was different for each scene, but *RECC* tends to produce stable results.
- *NCC* + *RECC* generates a larger number of successful matching points such that the bias compensation accuracy can be more improved by removing less reliable points and retaining a similar number of points to *RECC*.
- *NCC* + *RECC* can be a stable option to avoid potentially poorly accurate results, i.e., outliers.
- By applying the automated bias compensation, 1.1–1.2 pixels of accuracy in *RMSE* could be obtained.

Future studies should include the effects of parameters such as matching window size and search range for better image matching.

Acknowledgments

This study was supported by the Korea Aerospace Research Institute.

References

1 CEOS Analysis Ready Data: https://ceos.org/ard/ (accessed Jul. 1, 2023).
2 J. H. Jeong and T. J. Kim: ISPRS J. Photogramm. Remote Sens. **108** (2015) 172. https://doi.org/10.1016/j.isprsjprs.2015.07.006
3 J. Grodecki and G. Dial: Photogramm. Eng. Remote Sens. **69** (2003) 59. https://doi.org/10.14358/PERS.69.1.59
4 C. S. Fraser and H. B. Hanley: Photogramm. Eng. Remote Sens. **71** (2005) 909. https://doi.org/10.14358/PERS.71.8.909
5 Accuracy of world products: https://earth.esa.int/eogateway/missions/pleiades (accessed Apr. 22, 2024).
6 Pleiades instrument: https://earth.esa.int/eogateway/missions/pleiades (accessed Apr. 22, 2024).
7 J. H. Oh and C. N. Lee: ISPRS J. Photogramm. Remote Sens. **100** (2015) 14. https://doi.org/10.1016/j.isprsjprs.2014.02.009
8 W. Koppe, R. Wenzel, S. Hhnning, J. Janoth, P. Hummel, and H. Raggam: IEEE Int. Geoscience and Remote Sensing Symposium (2012) 3580. https://doi.org/10.1109/IGARSS.2012.6350643
9 L. Chandelier, L. Coeurdevey, S. Bosch, P. Fave, R. Gachet, A. Orsoni, T. Tilak, and A. Barot: ISPRS Ann. Photogramm. Remote Sens. Spatial Inf. Sci. **2** (2020) 15. https://doi.org/10.5194/isprs-annals-V-2-2020-15-2020
10 Y. Lee, J. Son, and T. Kim: Int. Archives of the Photogrammetry Remote Sensing and Spatial Information Sciences. **43** (2022) 287, https://doi.org/10.5194/isprs-archives-XLIII-B1-2022-287-2022
11 SEN3GCP: https://eo4society.esa.int/projects/sen3gcp/ (accessed Jul. 3, 2023).
12 Ground Control Point (GCP) Archive – Worldwide: https://www.esri.com/en-us/arcgis-marketplace/listing/products/8cc5f4ec414a40ed81ec46f7fbec8b11 (accessed Jul. 3, 2023).
13 P. Pehani, K. Čotar, A. Marsetič, J. Zaletelj, and K. Oštir: Remote Sens. **8** (2016) 343, https://doi.org/10.3390/rs8040343
14 X. Shen, Q. Li, G. Wu, and J. Zhu: Remote Sens. **9** (2017) 200, https://doi.org/10.3390/rs9030200
15 A. Marsetič and P. Pehani: Remote Sens. **11** (2019) 1097, https://doi.org/10.3390/rs11091097
16 J. H. Oh, D. C. Seo, C. N. Lee, S. K. Seong, and J. H. Choi: IEEE Access. **10** (2022). https://doi.org/10.1109/ACCESS.2022.3217788
17 P. Tang, K. Zheng, X. Shan, C. Hu, L. Huo, L. Zhao, and H. Li: J. Remote Sens. **20** (2016) 1126. https://www.researchgate.net/publication/309670983_Framework_of_remote_sensing_image_automatic_processing_with_invariant_feature_point_set_as_control_data_set
18 Y. K. Han and J. H. Oh: Sensors. **18** (2018) 1599. https://doi.org/10.3390/s18051599
19 D. G. Lowe: Int. J. Comput. Vision. **60** (2004) 91. https://doi.org/10.1023/B:VISI.0000029664.99615.94
20 H. Bay, A. Ess, T. Tuytelaars, and L. Van Gool: European Conf. Computer Vision part of the Lecture Notes in Computer Science LNIP. **3951** (2006) 404. https://doi.org/10.1007/11744023_32
21 A. Alahi, R. Ortiz, and P. Vandergheynst: Proc. 2012 IEEE Conf. Comp. Vis. Pattern Recog (CVPR, 2012) 510. https://ieeexplore.ieee.org/document/6247715
22 J. P. Lewis: Vision Interface **95** (1995) 120. https://citeseerx.ist.psu.edu/document?repid=rep1&type=pdf&doi=57d797a1389ed6211ef39e203eecabcd0d7e37e5
23 J. H. Oh, C. N. Lee, Y. Eo, and J. Bethel: Photogramm. Eng. Remote Sens. **78** (2012) 1045. https://doi.org/10.14358/PERS.78.10.1045
24 C. Tao and H. Yong: Photogramm. Eng. Remote Sens. **67** (2001) 1347. https://www.asprs.org/wp-content/uploads/pers/2001journal/december/2001_dec_1347-1357.pdf
25 J. Canny: IEEE Trans. Pattern Anal. Mach. Intell. **8** (1986) 679. https://doi.org/10.1109/TPAMI.1986.4767851
26 M. A. Fischler and R. C. Bolles: Communications of the ACM. **24** (1981) 381. https://doi.org/10.1145/358669.358692
27 W. Baarda: Netherlands Geodetic Commission (Delft, Netherlands) **2** (1968) 53.
28 D. C. Seo, G. B. Hong, and C. G. Jin: Proc. The 33rd Asian Conf. Remote Sensing (ACRS, 2015). https://repository.unpak.ac.id/tukangna/repo/file/files-20220224083937.pdf

About the Authors

Jaehong Oh received his B.S. and M.S. degrees in civil engineering from Seoul National University, Seoul, Korea, in 1999 and 2001, respectively, and his Ph.D. degree from Ohio State University, Columbus, OH, in 2011. He was a senior researcher at Space Imaging Asia and Electronics and Telecommunications Research Institute (ETRI) and now works as a professor in civil engineering at the Korea Maritime and Ocean University. His research interests cover georeferencing techniques, including photogrammetric sensor modeling and stereo image processing. (jhoh@kmou.ac.kr)

Doochun Seo received his Ph.D. degree in civil engineering from Gyeongsang National University, South Korea, in 2002. He has been with the Korea Aerospace Research Institute since 2002, and has also been a senior researcher with the Satellite Cal/Val Department since 2005. His primary research interests and background include satellite photogrammetry, sensor modeling, DEM, ortho-image generation, automated feature extraction from imagery, and the geometric calibration of high-resolution satellite image data. (dcivil@kari.re.kr)

Jaewan Choi received his B.S. and M.S. degrees in civil, urban, and geosystem engineering and his Ph.D. degree in civil and environmental engineering from Seoul National University, Seoul, Korea, in 2004, 2006, and 2011, respectively. He is currently a professor with the School of Civil Engineering, Chungbuk National University, Cheongju, Korea. His research interests include pansharpening, change detection, image registration, and deep-learning-based applications for satellite imagery. (jaewanchoi@chungbuk.ac.kr)

Youkyung Han received his B.S., M.S., and Ph.D. degrees in civil and environmental engineering from Seoul National University, Seoul, South Korea, in 2007, 2009, and 2013, respectively. He is currently an associate professor with the Department of Civil Engineering at Seoul National University of Science and Technology and also the head of the Remote Sensing Image Processing Laboratory, Seoul, South Korea. His major research interests include the image processing of very high resolution remote sensing data such as image registration, segmentation, object extraction, and change detection. (han602@seoultech.ac.kr)

Changno Lee received his B.S. and M.S. degrees in civil engineering from Seoul National University, Seoul, Korea, in 1987 and 1989, respectively, and his Ph.D. degree from Purdue University, West Lafayette, IN, USA, in 1999. He was a senior researcher at the Electronics and Telecommunications Research Institute and currently works as a professor in civil engineering at Seoul National University of Science and Technology. His research interests include sensor modeling, robust estimation, and automated feature extraction from imagery. (changno@seoultech.ac.kr)